ADVANCED MATERIALS

Supporting Information

for *Adv. Mater.*, DOI 10.1002/adma.202312008

Electrically Controlled All-Antiferromagnetic Tunnel Junctions on Silicon with Large Room-Temperature Magnetoresistance

Jiacheng Shi, Sevdenur Arpaci, Victor Lopez-Dominguez, Vinod K. Sangwan, Farzad Mahfouzi, Jinwoong Kim, Jordan G. Athas, Mohammad Hamdi, Can Aygen, Hanu Arava, Charudatta Phatak, Mario Carpentieri, Jidong S. Jiang, Matthew A. Grayson, Nicholas Kioussis*, Giovanni Finocchio*, Mark C. Hersam and Pedram Khalili Amiri**

Supplementary Information

Electrically controlled all-antiferromagnetic tunnel junctions on silicon with large room-temperature magnetoresistance

Jiacheng Shi[1=], Sevdenur Arpaci[1,2=], Victor Lopez-Dominguez[1,3], Vinod K. Sangwan[4], Farzad Mahfouzi[5], Jinwoong Kim[5], Jordan G. Athas[1], Mohammad Hamdi[1], Can Aygen[1], Hanu Arava[6], Charudatta Phatak[6], Mario Carpentieri[7], Jidong S. Jiang[6], Matthew A. Grayson[1,2], Nicholas Kioussis[5]*, Giovanni Finocchio[8]*, Mark C. Hersam[1,2,4,9], Pedram Khalili Amiri[1,2]**

Affiliations:

[1] Department of Electrical and Computer Engineering, Northwestern University; Evanston, Illinois 60208, United States of America.

[2] Applied Physics Program, Northwestern University; Evanston, Illinois 60208, United States of America.

[3] Institute of Advanced Materials (INAM), Universitat Jaume I; Castellón, 12006, Spain.

[4] Department of Materials Science and Engineering, Northwestern University; Evanston, Illinois 60208, United States of America.

[5] Department of Physics and Astronomy, California State University Northridge; Northridge, California 91330, United States of America.

[6] Materials Science Division, Argonne National Laboratory; Lemont, Illinois 60439, United States of America.

[7] Department of Electrical and Information Engineering, Politecnico di Bari; Bari, Italy.

[8] Department of Mathematical and Computer Sciences, Physical Sciences and Earth Sciences, University of Messina; Messina 98166, Italy.

[9] Department of Chemistry, Northwestern University; Evanston, Illinois 60208, United States of America.

* Email: victor.lopez@uji.es, nick.kioussis@csun.edu, gfinocchio@unime.it, pedram@northwestern.edu

[=] These authors contributed equally to this work.

The PDF file includes:

- Methods
- Supplementary Notes 1 to 6
- Figs. S1 to S9

Methods

Device fabrication: The materials used in this work were deposited on thermally oxidized silicon substrates under an Ar pressure of 2.5 mTorr at room temperature, in a sputtering system with base pressure less than 5×10^{-9} Torr. The $PtMn_3$ pillars with diameters of 6 and 8 μm were deposited by co-sputtering from Pt and Mn targets at nominal powers of 7 W and 150 W, respectively. A 2 nm Al layer was then deposited and oxidized in an oxygen plasma to obtain the Al_2O_3 tunnel barrier. Photolithography and dry etching processes were used to pattern the device structure and the contacts to the tunnel junction. Finally, Ti (10)/Al (80) electrodes were deposited by electron beam evaporation to form the electrical contacts of the device.

Electrical measurements: Electrical write current pulses were applied using a 6221 Keithley Current Source for all the measurements, as shown in Fig. 1 of the main text. The junction resistance was measured by applying a 10 μA current between electrodes 7 and 4, and then, measuring the voltage between electrodes 8 and 1 using a Keithley 2182A nano-voltmeter operating in the delta mode option. The 6-terminal differential voltage measurements were carried out by applying a reading current of 10 μA between electrodes 1 and 4. The differential voltage was then measured between electrodes 5 and 6 using a Keithley 2182A nano-voltmeter operating in the delta mode option.

X-ray diffraction (XRD) measurements: Additional 10 nm thick $PtMn_3$ layers (with the same growth method described in the device fabrication section above) on 5 nm Pt layers were sputtered on a thermally oxidized silicon substrate to analyze their crystal structure. X-ray diffraction measurements were performed in a Rigaku SmartLab system, the results of which are shown in Supplementary Note 1 and Fig. S1B.

X-ray photoelectron spectroscopy (XPS) measurements: XPS spectra were measured on a $PtMn_3$ reference layer to confirm its composition, using a Thermo Scientific ESCALAB 250Xi X-ray Photoelectron Spectrometer. The XPS results are shown in Supplementary Note 1 and Fig. S1A.

Density functional theory simulations: We performed structural relaxations using the Vienna ab-initio Simulation Package (VASP) code [1-3] on a $PtMn_3$[111] layer, 4 nm in thickness, interfaced with a 1.7 nm thick α-Al_2O_3 layer. The system was treated with a periodic boundary condition along the c axis, namely no vacuum was included. The hexagonal in-plane lattice constant was fixed at 5.29 Å, which corresponds to the bulk $PtMn_3$. We minimized the total energy with respect to the amplitude of the lattice vector c. The relaxation was performed using the Perdew-Burke-Ernzerhof (PBE) [4] exchange correlation functional and a 6 × 6 × 1 Γ centered *k*-points mesh with spin-orbit coupling. Using the relaxed coordinates of $PtMn_3$/α-Al_2O_3, we employed the OpenMX DFT package [5-7] to obtain the Hamiltonian in the atomic orbital basis sets. A 11× 11 × 1 *k*-points mesh was used for the self-consistent field (SCF) calculation. The unit cells in the middle of the $PtMn_3$ film were utilized to calculate the self-energies of the left and right leads. The self-energies were calculated using the Sancho-Rubio fast recursive method [8]. The $PtMn_3$ film was divided in half by removing the hopping elements between the top and bottom halves. The lead self-energies were added to the corresponding surface layers to extend them into the semi-infinite limit. In the case of the anti-parallel configuration, we multiplied the exchange splitting of one side of the junction by a negative sign. Subsequently, the Landauer-Buttiker formula [9] was employed to calculate the transmission across the AATJ for both parallel T_P and anti-parallel T_{AP} cases. A

51×51×1 *k*-points mesh was used for the transmission calculations.

Micromagnetic model: The micromagnetic simulations were performed using a well-established two-sublattice micromagnetic solver which solves two Landau-Lifshitz-Gilbert-Slonczewski (LLGS) equations [10-14], strongly coupled through the exchange interactions,

$$\begin{cases} \dfrac{d\boldsymbol{m}_1}{dt} = -\gamma_0 \boldsymbol{m}_1 \times \boldsymbol{H}_{eff,1} + \alpha \boldsymbol{m}_1 \times \dfrac{d\boldsymbol{m}_1}{dt} + \boldsymbol{\tau}_{SH,1} \\ \dfrac{d\boldsymbol{m}_2}{dt} = -\gamma_0 \boldsymbol{m}_2 \times \boldsymbol{H}_{eff,2} + \alpha \boldsymbol{m}_2 \times \dfrac{d\boldsymbol{m}_2}{dt} + \boldsymbol{\tau}_{SH,2} \end{cases} \tag{1}$$

where $\boldsymbol{m}_1$ and $\boldsymbol{m}_2$ are the two sub-lattice magnetizations, γ_0 is the gyromagnetic ratio, and α is the Gilbert damping parameter,

$$\boldsymbol{\tau}_{SH,i} = -\gamma_0 H_{SH}\, \boldsymbol{m}_i \times \left(\boldsymbol{m}_i \times \boldsymbol{p}\right) \tag{2}$$

is the Slonczewski-like SOT, associated mainly with the spin-Hall effect, with the amplitude given by $H_{SH} = \hbar \theta_{SH} J / \left(2et\mu_0 M_S\right)$ [12]. In the last expression, $\hbar$, θ_{SH}, $e<0$, t, and μ_0 are the reduced Planck's constant, the spin Hall angle, the electron charge, the AFM film thickness, and the vacuum permeability respectively, while J is the applied current density. The saturation magnetization is equal in both sublattices $M_{S1} = M_{S2} = M_S$. The direction of the spin polarization is $\boldsymbol{p} = \boldsymbol{z} \times \boldsymbol{j}$ (see Fig. 1 in the main text), $\boldsymbol{j}$ being the unit vector of the current density direction.

We consider a face-centered cubic unit cell with lattice constant a = 0.38 nm for the $PtMn_3$, where only the Mn atoms are magnetic. Therefore, the magnetic unit cell is a bcc cell with a lattice constant $a_m = a/\sqrt{2} = 0.28$ nm. $\boldsymbol{H}_{eff,1}$ and $\boldsymbol{H}_{eff,2}$ are the effective fields for the first and second sublattice, respectively. They include the anisotropy field (see Eq. 4), the demagnetizing term, and the exchange field, which is given by three contributions:

$$\begin{aligned} \boldsymbol{H}_{1,\mathrm{exch}} &= \frac{2A_{11}}{\mu_0 M_s}\nabla^2 \boldsymbol{m}_1 + \frac{4A_0}{a_m{}^2 \mu_0 M_s}\boldsymbol{m}_2 + \frac{A_{12}}{\mu_0 M_s}\nabla^2 \boldsymbol{m}_2, \\ \boldsymbol{H}_{2,\mathrm{exch}} &= \frac{2A_{11}}{\mu_0 M_s}\nabla^2 \boldsymbol{m}_2 + \frac{4A_0}{a_m{}^2 \mu_0 M_s}\boldsymbol{m}_1 + \frac{A_{12}}{\mu_0 M_s}\nabla^2 \boldsymbol{m}_1. \end{aligned} \tag{3}$$

Here, a_m is the magnetic lattice constant and A_{11}, A_0, A_{12} are the inhomogeneous intra-lattice, homogeneous inter-lattice and inhomogeneous inter-lattice exchange constants characterizing the interaction [12]. Finally, the cubic anisotropy field can be written as

$$\boldsymbol{H}_{anis} = m_u\left(m_v^2 + m_w^2\right)\boldsymbol{u} + m_v\left(m_u^2 + m_w^2\right)\boldsymbol{v} + m_w\left(m_u^2 + m_v^2\right)\boldsymbol{w}\ , \tag{4}$$

where $\boldsymbol{u}, \boldsymbol{v}, \boldsymbol{w}$ are the unit vectors of the crystallographic reference system [10].

The inhomogeneous intra-lattice exchange constant is $A_{11} = 0.8 \times 10^{-11}\, J/m$, and both the homogeneous and inhomogeneous inter-lattice exchange constants are $A_0 = A_{12} = -1.0 \times 10^{-11}\, J/m$. We considered the damping parameter to be α= 0.05, while the spin Hall angle is θ_{SH} = 0.1. The saturation magnetization of Mn was considered to be M_S = 153.75 kA/m. The cubic anisotropy constant is $K_C = -0.62 \times 10^6\, J/m^3$. Figure S5 shows an example of the simulated equilibrium configuration of one sublattice magnetization. The red (blue) color in the figure refers to the positive (negative) out-of-plane component of the magnetization along the z-axis.

Supplementary Note 1. Structural and magnetic characterization results

Additional Pt(5 nm)/$PtMn_3$(10 nm) bilayers were sputter deposited on a thermally oxidized silicon substrate to analyze their crystal structure and composition. The x-ray diffraction pattern (Fig. S1B) shows that the $PtMn_3$ film is in the noncollinear $L1_2$ phase, which has a magnetic Kagome-like lattice. In addition, the $PtMn_3$ layer is texturized in the [111] direction, following the underlying Pt layer, as also indicated by the HRTEM results shown in the main text (Fig. 1C). XPS measurements conducted in an additional $PtMn_3$ (20 nm) layer revealed the 2p-Mn and 4f-Pt peaks, which indicate a Mn:Pt ratio of ~ 3.2. These XPS results are shown in Fig. S1A.

In order to confirm the antiferromagnetic order of our $PtMn_3$ films, we constructed additional Pt(5)/$PtMn_3$(10)/Pt(1)/Co(1.2)/Pt(2) (thicknesses in nanometers) multilayers, using the same deposition conditions as the $PtMn_3$ layers described in the main text. The hysteresis loop, shown in Fig. S2, was measured using a vibrating sample magnetometer (VSM), by applying a magnetic field along the sample plane between -300 and 300 Oe, and indicates an exchange bias field of approximately 30 Oe. The 1 nm Pt insertion layer was used to prevent diffusion of Mn atoms into the Co layer. The presence of in-plane exchange bias further confirms the non-collinear spin configuration of $PtMn_3$ constrained in the [111] plane.

The noncollinear phase of $PtMn_3$ also exhibits an anomalous Hall effect (AHE) [15]. We measured such an AHE signal in Hall bars of Pt/$PtMn_3$ with a width of 20 μm, which were fabricated under the same conditions as the samples in the main text. These results, which are shown in Fig. S2B, confirm the presence of the noncollinear antiferromagnetic phase in our samples.

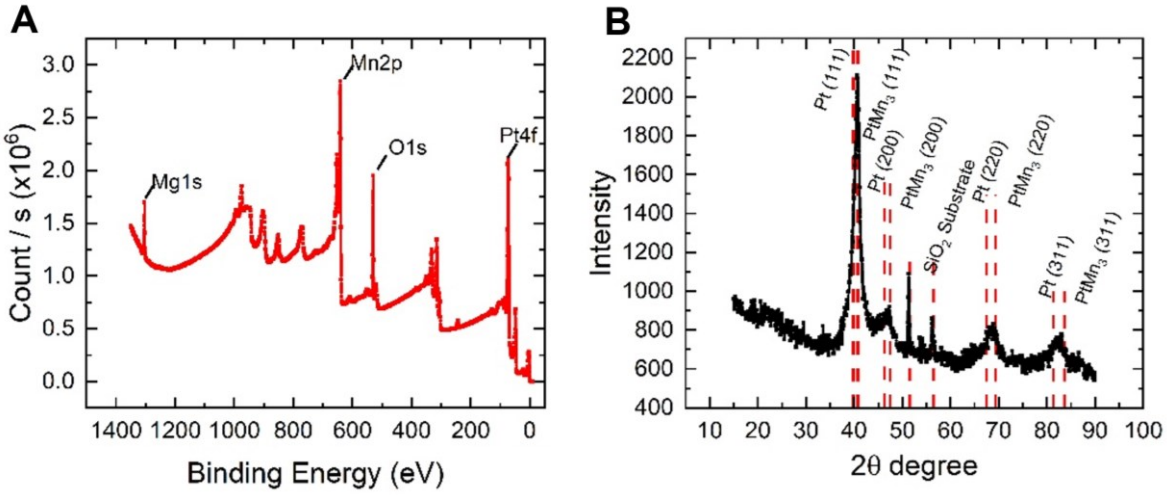

Fig. S1. X-ray photoelectron spectroscopy (XPS) and X-ray diffraction (XRD) measurements in $PtMn_3$ layers grown using the same method as those in the main text. A, XPS measurements for a $PtMn_3$ (20 nm) layer capped with MgO. The XPS peak analysis reveals a ~ 3.2 ratio of Mn:Pt. **B,** XRD measurements performed in a Pt (5 nm) / $PtMn_3$ (10 nm) bilayer capped with MgO, confirming the antiferromagnetic $L1_2$ phase of the $PtMn_3$ layer.

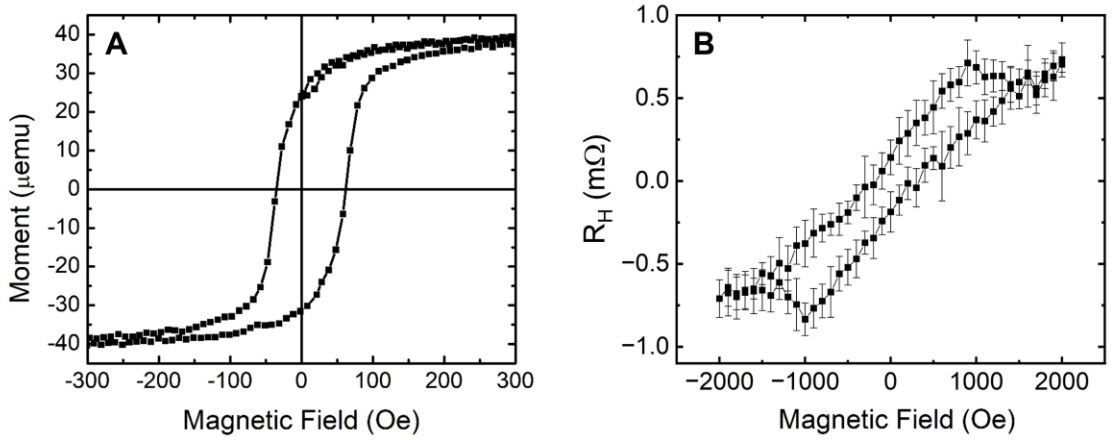

Fig. S2. A, In-plane VSM measurement of Pt(5)/$PtMn_3$(10)/Pt(1)/Co(1.2)/Pt(2) (thicknesses in nanometers) in the field range between -300 Oe to 300 Oe, indicating an exchange bias field of approximately 30 Oe. **B,** Anomalous Hall effect measurements as a function of an out-of-plane applied field in Hall bars of Pt/$PtMn_3$, where R_H indicates the anomalous Hall resistance value after subtraction of a constant background.

Supplementary Note 2. TR measurements on additional three-terminal AATJ devices

We measured 12 devices in total, all of which exhibited qualitatively similar behavior. The distribution of $\Delta R/R$ and ΔR values for all these devices is summarized in Fig. 5 of the main text. Figure S3 shows data for two additional devices, both having an AATJ diameter of 8 μm, which exhibit $\Delta R/R$ values ~35% and ~50%, respectively. The procedure used for these current-induced switching measurements was the same as shown in the main text. It is worth noting that in some of the measured devices (see Fig. S3A), the switching signal develops only after an initial series of unsuccessful switching attempts. We hypothesize that this originates from the heating of the devices during the first few current pulse cycles. Note also that some of the devices show more than two resistance levels, which is expected to emerge from the multi-domain structure of these relatively large-diameter pillars. This hypothesis is supported by micromagnetic simulations, which are shown in Supplementary Note 4.

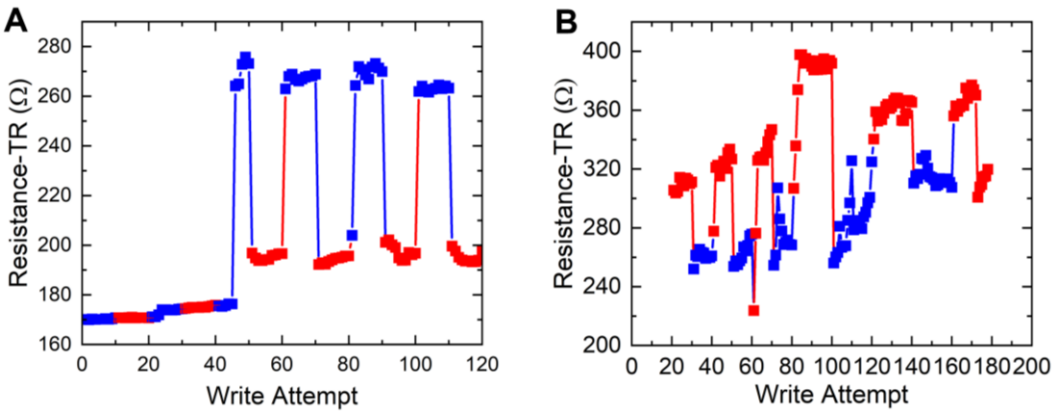

Fig. S3. Current-induced switching measurements on two additional AATJ devices with 8μm diameter, which exhibit $\Delta R/R$ values of ~35% (**A**) and ~50% (**B**), respectively.

Supplementary Note 3. TR measurements on a non-magnetic $Pt/Al_2O_3/Pt$ control device

We fabricated additional tunnel junction control devices, where the AFM layers were replaced by a Pt layer of the same thickness, which was subsequently patterned into a pillar of 8 μm diameter. The electrical current-induced switching experiments on these control devices were performed in the same way as those described in the manuscript. None of the measured control devices exhibited a resistive switching signal for the range of currents used in our AATJ switching experiments. A representative curve is shown in Fig. S4. These control experiments confirm the magnetic origin of the switching signal observed in our $PtMn_3$-based tunnel junctions.

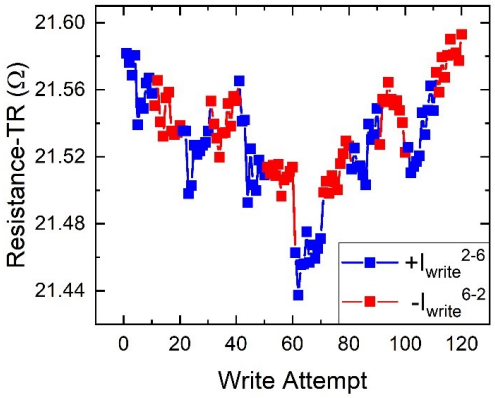

Fig. S4. Control experiment in Pt-only tunnel junction devices. No resistive switching signals were observed in control tunnel junction devices made without the $PtMn_3$ free layer.

Supplementary Note 4. Micromagnetic simulation results

To evaluate the effect of material imperfections on the switching characteristics, we perfomed a study of the effect of the pinning potential, emerging from local variations of anisotropy within the $PtMn_3$ layer. The anisotropy constant of each grain was assumed to follow a Gaussian distribution with mean $K_C = -0.62\ x\ 10^6\ J/m^3$ and standard deviation σ. In particular, we considered a Voronoi map with a given grain distribution, where the average diameter of the grains was 10 nm. We then changed the standard deviation of the anisotropy, ranging from $\sigma = 0.02$ to $\sigma = 0.15$. As a result, each grain in the simulation showed a different anisotropy constant. Figure S6A shows the threshold current density necessary to move the domain wall shown in Fig. S5 from its pinning site, as a function of the standard deviations of the anisotropy constant. This threshold current density is 8 MA/cm^2 for $\sigma = 0.02$, which increases to 65 MA/cm^2 at $\sigma = 0.15$.

This result allows one to qualitatively understand the device-to-device variations of switching characteristics in our devices, which may emerge from film nonuniformities induced during material growth or subsequent device fabrication steps. Specifically, increased pinning potentials in the film lead to a larger threshold current density, thereby giving rise to incomplete switching for the same applied current. Figures S6B-D show snapshots of the domain wall displacement from the equilibrium position for different current densities (J = 10, 15, and 20 MA/cm^2, for the panels B-D, respectively) when the Voronoi deviation is $\sigma = 0.05$. In each case, the domain wall gets pinned to a different location on the nanowire where the pinning potential is higher, the location of which depends on the value of the current density. Qualitatively similar results were observed for different grain distributions.

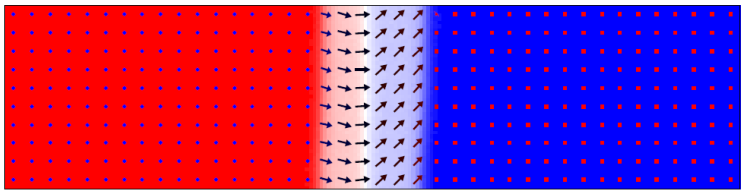

Fig. S5. Snapshot of the first sublattice magnetization depicting a possible ground state of the magnetization in a nanowire device. The red (blue) color denotes the positive (negative) out-of-plane component of the magnetization.

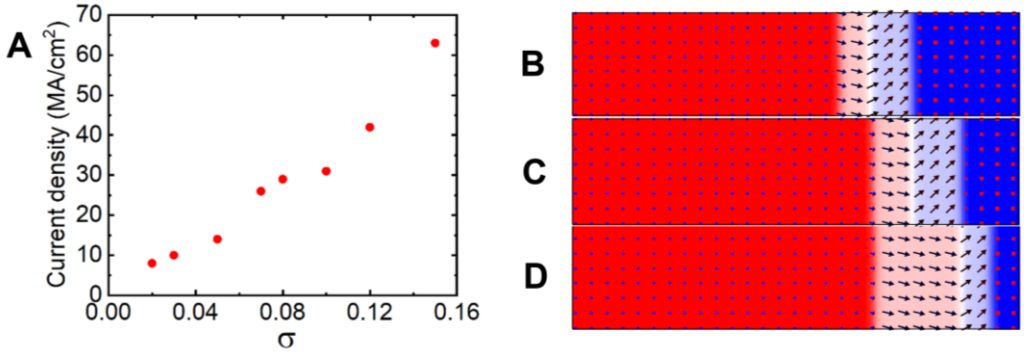

Fig. S6. A, Threshold current density required to move the domain wall shown in Fig. S5, as a function of the standard deviation of the anisotropy constant (σ). **B-D,** Snapshots of the first sublattice magnetization when a current density of $J = 10$, 15, and 20 MA/cm^2 is applied for panels B-D, respectively. The calculations were performed with a standard deviation $\sigma = 0.05$.

Supplementary Note 5. High-resolution XRD measurements

To better separate the [111] peaks from $PtMn_3$ and Pt in Fig. S1B, we deposited additional samples of SiO_2/Pt(5)/$PtMn_3$(10) and SiO_2/Pt(5)/$PtMn_3$(20) (thickness in nanometers), and performed high-resolution XRD measurements for $35 \leq 2\theta \leq 55$ degrees on them. The results are shown in Fig. S7.

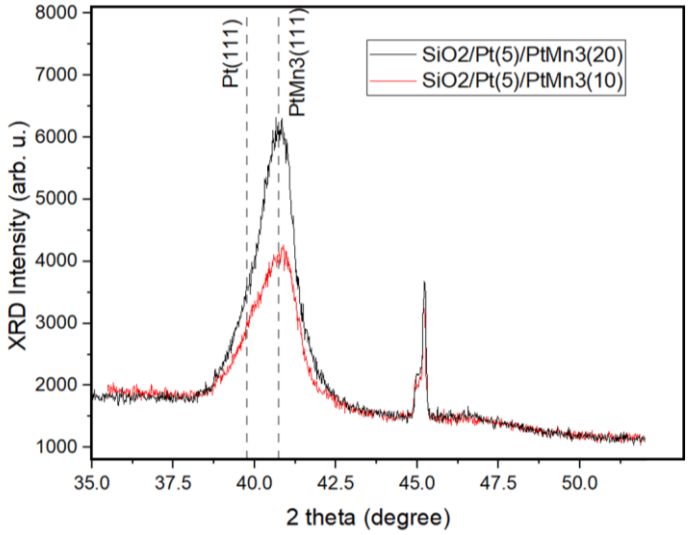

Fig. S7. XRD measurements for two Pt/$PtMn_3$ samples having different $PtMn_3$ thickness.

The intensity of the observed peak is higher in the 20 nm sample, which indicates that the peak originates primarily from $PtMn_3$. A linear baseline was subtracted from the raw data for both samples. Due to the broadening of the peaks, it is not possible to observe two distinct peaks for Pt [111] and $PtMn_3$ [111] as they are separated only by $\Delta(2\theta) = 0.976$ degrees. However, the data for both samples indicate an asymmetric peak (due to the overlap of two broad peaks). The baseline-subtracted data for both samples were fitted with two Gaussian peaks. The results are shown in Fig. S8 for the case of the 10 nm $PtMn_3$ sample. The bulk values of 2θ from the [111] planes from both materials are indicated by the dashed lines, which confirm that the larger [111] peak observed in our data indeed originates from $PtMn_3$.

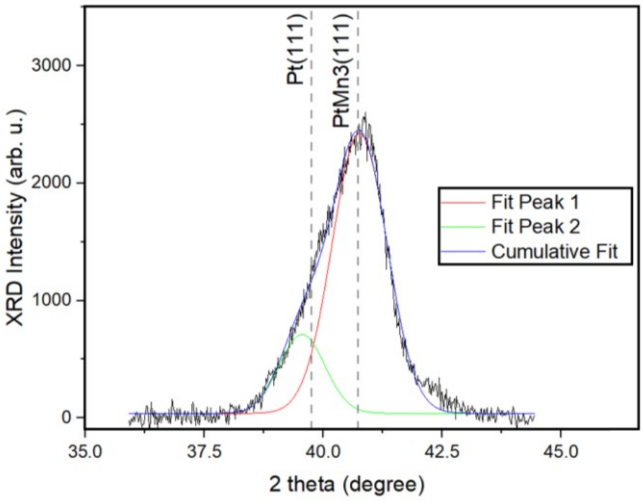

Fig. S8. Gaussian fits to the Pt(5)/$PtMn_3$(10) XRD data. Dashed lines show the expected (bulk) positions of the Pt and $PtMn_3$ peaks.

Supplementary Note 6. TEM nano-beam diffraction analysis

To further confirm the intended [111] texture in both $PtMn_3$ layers, we additionally collected electron diffraction patterns from local regions in the sample. This nano-beam diffraction analysis confirms that there is a strong [111] preferred orientation, as shown in Fig. S9, in agreement with the XRD results and the TEM results shown in the main text.

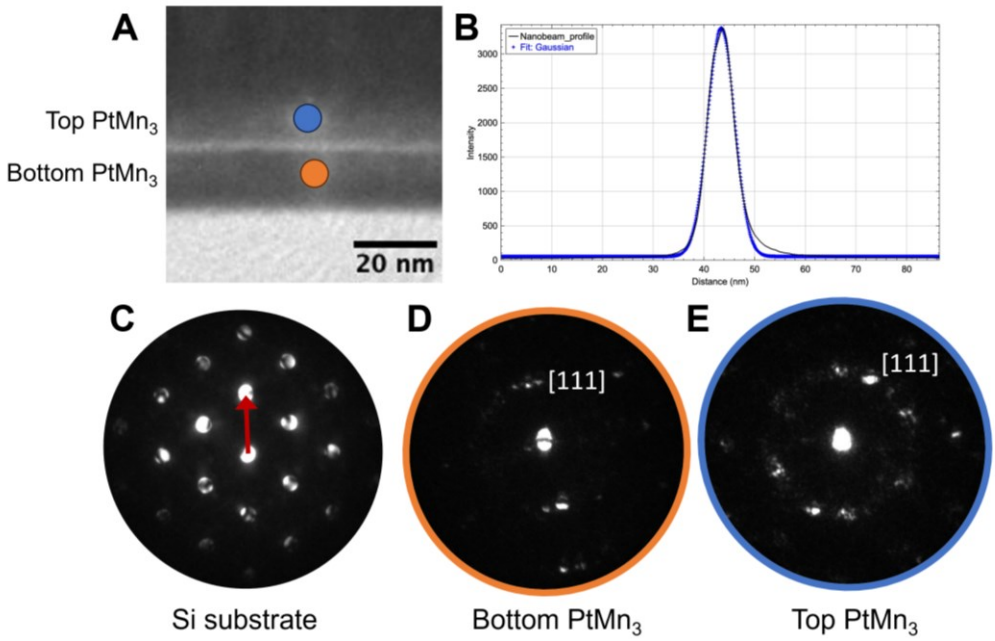

Fig. S9. A, TEM image showing the tunnel junction with the blue and orange dots indicating the position of the beam during nanobeam diffraction. **B,** Profile of the electron beam with a Gaussian fit indicating a 6.5 nm full-width half-maximum (FWHM). **C,** Nanobeam diffraction pattern from the Si substrate with the red arrow indicating the surface normal (film growth) direction. **D** and **E,** Nanobeam diffraction patterns from the bottom and top $PtMn_3$ layers, respectively, showing strong [111] spots along the surface normal, indicating the preferred orientation during growth.

References

[1] Kresse, G.; Joubert, D., From ultrasoft pseudopotentials to the projector augmented-wave method. *Physical Review B* **1999,** *59*, 1758-1775.

[2] Kresse, G.; Furthmüller, J., Efficient iterative schemes for ab initio total-energy calculations using a plane-wave basis set. *Physical Review B* **1996,** *54*, 11169-11186.

[3] Kresse, G.; Furthmüller, J., Efficiency of ab-initio total energy calculations for metals and semiconductors using a plane-wave basis set. *Computational Materials Science* **1996,** *6*, 15-50.

[4] Perdew, J. P.; Burke, K.; Ernzerhof, M., Generalized Gradient Approximation Made Simple. *Physical Review Letters* **1996,** *77*, 3865-3868.

[5] Ozaki, T., Variationally optimized atomic orbitals for large-scale electronic structures. *Physical Review B* **2003,** *67*, 155108.

[6] Ozaki, T.; Kino, H., Numerical atomic basis orbitals from H to Kr. *Physical Review B* **2004,** *69*, 195113.

[7] Ozaki, T.; Kino, H., Efficient projector expansion for the ab initio LCAO method. *Physical Review B* **2005,** *72*, 045121.

[8] Sancho, M. L.; Sancho, J. L.; Rubio, J., Quick iterative scheme for the calculation of transfer matrices: application to Mo (100). *Journal of Physics F: Metal Physics* **1984,** *14*, 1205.

[9] Meir, Y.; Wingreen, N. S., Landauer formula for the current through an interacting electron region. *Physical Review Letters* **1992,** *68*, 2512-2515.

[10] Arpaci, S.; Lopez-Dominguez, V.; Shi, J.; Sánchez-Tejerina, L.; Garesci, F.; Wang, C.; Yan, X.; Sangwan, V. K.; Grayson, M. A.; Hersam, M. C., Observation of current-induced switching in non-collinear antiferromagnetic $IrMn_3$ by differential voltage measurements. *Nature*

communications **2021,** *12*, 1-10.
[11] Tomasello, R.; Verba, R.; Lopez-Dominguez, V.; Garesci, F.; Carpentieri, M.; Di Ventra, M.; Khalili Amiri, P.; Finocchio, G., Antiferromagnetic Parametric Resonance Driven by Voltage-Controlled Magnetic Anisotropy. *Physical Review Applied* **2022,** *17*, 034004.
[12] Puliafito, V.; Khymyn, R.; Carpentieri, M.; Azzerboni, B.; Tiberkevich, V.; Slavin, A.; Finocchio, G., Micromagnetic modeling of terahertz oscillations in an antiferromagnetic material driven by the spin Hall effect. *Physical Review B* **2019,** *99*, 024405.
[13] Landau, L. D.; Lifshitz, E. M., On the theory of the dispersion of magnetic permeability in ferromagnetic bodies. *Physik. Zeits. Sowjetunion* **1935,** *8*, 153.
[14] Gilbert, T. L., A phenomenological theory of damping in ferromagnetic materials. *IEEE Transactions on Magnetics* **2004,** *40*, 3443-3449.
[15] Liu, Z. Q.; Chen, H.; Wang, J. M.; Liu, J. H.; Wang, K.; Feng, Z. X.; Yan, H.; Wang, X. R.; Jiang, C. B.; Coey, J. M. D.; MacDonald, A. H., Electrical switching of the topological anomalous Hall effect in a non-collinear antiferromagnet above room temperature. *Nature Electronics* **2018,** *1*, 172-177.